Computers, Materials & Continua

Tech Science Press

Doi:10.32604/cmc.2025.070707

ARTICLE

Porosity-Impact Strength Relationship in Material Extrusion: Insights from MicroCT, and Computational Image Analysis

Jia Yan Lim[1,2], Siti Madiha Muhammad Amir[3], Roslan Yahya[3], Marta Peña Fernández[2] and Tze Chuen Yap[1,*]

[1]School of Engineering and Physical Sciences, Heriot-Watt University Malaysia, Putrajaya, 62200, Malaysia
[2]School of Engineering and Physical Sciences, Heriot-Watt University, Edinburgh, EH14 4AS, UK
[3]Industrial Technology Division, Malaysian Nuclear Agency, Kajang, 43000, Malaysia

*Corresponding Author: Tze Chuen Yap. Email: t.yap@hw.ac.uk

Received: 22 July 2025; Accepted: 23 October 2025; Published: 09 December 2025

ABSTRACT: Additive Manufacturing, also known as 3D printing, has transformed conventional manufacturing by building objects layer by layer, with material extrusion or fused deposition modeling standing out as particularly popular. However, due to its manufacturing process and thermal nature, internal voids and pores are formed within the thermoplastic materials being fabricated, potentially leading to a decrease in mechanical properties. This paper discussed the effect of printing parameters on the porosity and the mechanical properties of the 3D printed polylactic acid (PLA) through micro-computed tomography (microCT), computational image analysis, and Charpy impact testing. The results for both tests were correlated to investigate the relationship between porosity and Charpy impact strength. PLA samples of 1 cm^3 × 1 cm^3 × 1 cm^3 were 3D printed at printing temperatures of 180°C, 200°C, 220°C, and 240°C, and at printing speeds of 50, 80, and 110 mm/s, while porosity was measured from microCT-reconstructed data. Additionally, impact strength was assessed using a notched Charpy impact tester following ASTM D6610-18. In general, results show that higher printing temperatures and lower printing speeds reduced pore size by improving material flow and fusion, while also increasing impact strength due to better thermal bonding and interlayer adhesion. A maximum 36.8% reduction in mean pore size and a 114% improvement in impact strength were observed at 110 mm/s and 220°C. Conversely, increasing printing speed led to lower Charpy impact strength. Optimal impact behavior and minimal voids were observed at a printing temperature of 220°C and a printing speed of 50 mm/s.

KEYWORDS: Additive manufacturing; fused filament fabrication; fused deposition modeling; material extrusion; 3D porosity; impact strength; polylactic acid

1 Introduction

The Fourth Industrial Revolution, Industry 4.0 (I4.0), signifies the merging of information and communication technologies (ICT) with the automation of machinery and manufacturing infrastructure on a broad scale to enhance industrial vitality. Within this paradigm, additive manufacturing (AM), colloquially known as 3D printing, has emerged as a pivotal component, revolutionizing traditional manufacturing processes by enabling layer-by-layer fabrication to produce advanced and custom-designed items. This technology not only facilitates intricate design realization but also streamlines production through the direct translation of digital models into physical objects, thereby redefining the boundaries of manufacturing efficiency and versatility [1].

Among various AM techniques, material extrusion (MEX/TRB-P), also known as fused deposition modeling (FDM), stands out for its widespread adoption and applicability [2]. By extruding thermoplastic filaments, this method enables rapid prototyping and production of diverse geometries with notable cost-effectiveness [3]. However, the optimization of printing parameters remains a critical issue to ensure the quality and reliability of printed components. One of the paramount concerns in extrusion 3D printing is the porosity, which can significantly compromise structural integrity and functional performance. Porosity results from incomplete fusion or air entrapment due to uncontrollable pressure after material deposition, as well as the choice of infill patterns during printing [4], remaining a pervasive challenge that necessitates investigation.

The resulting voids in 3D-printed materials have a significant impact on the quality and performance of the 3D-printed object. These voids are identified in three key regions within the structure of additively manufactured components: within the bulk material, between deposited layers, and at the fibre/matrix interface [5]. The fundamental cause of void formation is the uncontrollable pressure that occurs after the melted material leaves the printing head. The uncontrolled pressures with rapidly decreasing temperatures, can lead to insufficient bonding between material strands, as shown in Fig. 1. The cross-sectional shape of the material tracks deposited during printing, as well as the geometry and distribution of voids within MEX/TRB-P components are affected by parameters such as nozzle shape, material properties, temperature, flow rate, and deposition speed [4].

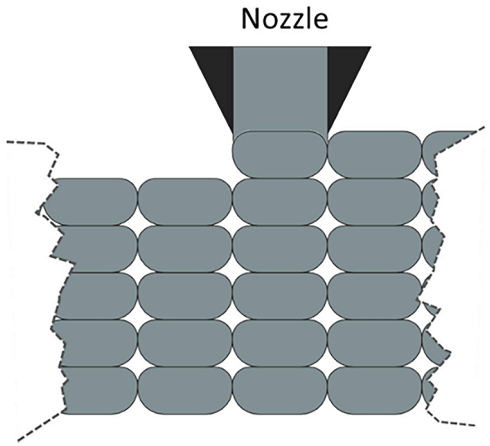

Figure 1: Formation of voids between material strands during material extrusion [6]

The mechanical properties of printed materials are another key factor in their suitability for various applications. While it is established that printing parameters impact mechanical properties [5,7–10]. The precise influence of these parameters on the underlying structural factors affecting mechanical properties remains unclear. This lack of clarity complicates the selection of printing parameters for achieving optimal mechanical properties [11]. Exploring the influence of printing parameters on mechanical performance and understanding the interplay between printing conditions and resultant porosity within printed objects becomes imperative to optimize material utilization and enhance component reliability.

Printing parameters such as infill density, printing temperature, and printing speed contribute to the formation and distribution of voids in 3D-printed parts. Direction-parallel patterns may have high density but could leave gaps in non-polygonal curvilinear layers, while contour-parallel patterns, tracing the perimeter, work well for such layers but might lead to voids within the contour due to filling challenges [12].

Higher printing speeds result in larger voids in polylactic acid (PLA) printed samples [13], whereas higher printing temperatures result in smaller voids and lower porosity [14].

Similarly, these printing parameters significantly influence the overall mechanical performance of 3D-printed PLA, with tensile strength decreasing at higher printing speeds [15]. In general, increasing printing speed during MEX 3D printing reduces voids between beads and contributes to a stronger printed part [16]. Opposite results were reported by Natarajan et al. [17], where they investigated the effect of printing speed and layer thickness on the mechanical properties of *Acacia concinna*-filled PLA. Their results showed that increasing printing speed reduced tensile, flexural, and impact strength. Furthermore, printing speed affects the cooling time and eventually affects the crystallinity of the printed part [16].

On the other hand, an increase in printing temperature results in an increase in tensile strength [14,16,18], bending strength [14], adhesion strength [19], strain at failure [20], wear resistance, and friction coefficient [21]. The correct extrusion or printing temperature is important to obtain good adhesion between the deposited beads, and high temperatures over the optimal limit reduce the strengths [16,22]. This suggests a strong dependence of the mechanical properties of printed samples on the printing temperature. However, research by Sultana et al. [23] indicates that the nozzle temperature and printing speed had relatively minor effects compared to other parameters, based on Analysis of variance (ANOVA) analysis, where the printing temperatures used were 180°C, 185°C, and 190°C, and the printing speeds were 10, 15, and 20 mm/s.

The presence of porosity significantly impacts the mechanical properties of 3D-printed samples, typically resulting in a weakening of the material. Variations in the size and shape of inter-bead pores are a crucial determinant of mechanical reliability. Several studies have investigated the relationship between porosity and impact strength in 3D-printed parts, showing that higher porosity content generally leads to decreased mechanical properties in the specimens, including tensile strength, Young's modulus, Poisson's ratio, compressive strength, and damping capacity [24]. The presence of porosity diminishes the mechanical properties of the specimens, as it initiates the failure process from the formation of voids.

Micro-computed tomography (microCT) serves as a quantitative and qualitative tool to assess deviations from ideal geometry and to understand how printing parameters affect surface roughness and interior characteristics. This quality assessment ensures safety and performance requirements in 3D-printed objects [25]. In addition, microCT assists in the investigation of porosity, cell shape, and internal and external surface roughness in complex 3D-printed objects [26]. The technology quantifies porosity and provides information about overall structural integrity and the extent and distribution of interior defects (Fig. 2). The mircoCT technique has been used for void measurement of material extrusion 3D-printed parts [27–31].

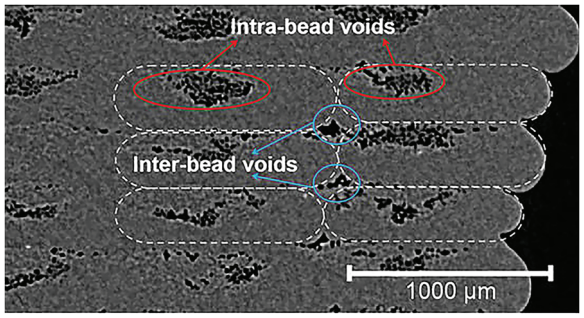

Figure 2: Micro-CT image of printed objects containing different types of voids: intra-bead (red) and inter-bead (blue) voids [32]

The effect of printing parameters (nozzle temperature, printing speed, raster angle, infill density, bed temperature, and layer thickness) on the porosity, surface roughness, and dimensional accuracy of MEX 3D-printed PLA has been previously investigated [27]. In that study [27], the research team utilized an L25 Taguchi orthogonal array to investigate the interaction effects of the printing parameters on three responses. MicroCT was used to measure the porosity of the prints. However, due to the large number of results, only five samples of microCT results were presented, selected from the diagonal of the (5 × 5) 25 cases. As such, the direct relationship between individual printing parameters, such as nozzle temperature and porosity, was not explicitly discussed. Since the work focused on statistical analysis of the results, the understanding of how porosity is linked to single printing parameters remains limited. Furthermore, the study did not examine the mechanical properties of the 3D prints.

A similar L25 orthogonal array investigation with the same six printing parameters and three responses was repeated on ABS [28]. Based on the ANOVA, regression equations were formed for optimizing these quality features and enhancing the overall performance of 3D-printed parts. This work also focused on statistical analysis of the results and did not explicitly discuss the underlying mechanisms.

The mechanical properties, thermal properties, structural characteristics, dimensional variance, and porosity of ferronickel slag (FNS)-PLA composite with six different weight percentages of FNS [2,4–6,10,14] were investigated by Vidakis et al. [31]. The authors used microCT to measure the porosity in the 3D prints, and showed that the inclusion of FNS particles reduced the porosity of the 3D-printed samples. The porosity of the composite first decreased with increasing weight percentage of FNS until 5% and after 5% the porosity increased. Furthermore, when the porosity of the PLA composite was the lowest porosity (at PLA-5% FNS), the tensile, flexural, and impact strengths were optimal. Similar work was reported by Petousis et al., where the mechanical properties and porosity of 3D-printed material extrusion of recycled fine powder glass (RFPG)-PLA composites of different weight percentages were investigated [30]. MicroCT images revealed that the porosity decreased as the RFPG content increased from 0% to 6% and after 6%, the porosity increased. Similarly, the optimal Charpy impact strength, flexural strength, and tensile strength occurred when the porosity was the lowest (at 6% RFPG).

In a recent study, the linkage between printing parameters, voids, and tensile properties of MEX-printed PLA was investigated by Faizaan et al. [29]. The authors conducted two Taguchi L9 DOE experiments to investigate the effects of three printing parameters, where the first case consisted of nozzle diameter, layer thickness, and extrusion temperature, while the second case consisted of layer thickness, print speed, and number of top/bottom layers. MicroCT scans were acquired for samples with varying nozzle diameters printed at a constant layer thickness of 0.15 mm and for samples of varying layer thickness printed at a constant nozzle diameter of 0.6 mm. From the microCT results, the authors reported that the lower layer thicknesses and larger nozzle diameters generated fewer voids, and eventually the lower void content produced better tensile properties.

Although there is extensive research on the effects of printing parameters on porosity and the link between porosity and mechanical properties, few studies have specifically investigated the relationship between impact strength and porosity in MEX/TRB-P 3D-printed PLA at different printing parameters, measured via microCT. Moreover, existing research often overlooks the influence of printing parameters when assessing the influence of porosity on mechanical properties (environmentally, sustainability). As a result, the interactions between printing parameters, porosity characteristics, and impact performance are not fully understood. In this study, the porosity in MEX/TRB-P printed PLA parts at three printing speeds and four different temperatures is measured via micro-CT image analysis, and the Charpy impact strengths of the prints are determined through Charpy impact testing. The relationship between printing parameters (printing speed, printing temperature), porosity, and impact strength is then evaluated.

2 Methodology

Fig. 3 shows the process, which begins with MEX/TRB-P 3D printing of PLA, where different printing parameters are systematically varied to observe their impact. Then, the specimens undergo two parallel assessments. The first involves the identification of voids within the 3D-printed samples using microCT scanning. In parallel, MEX/TRB-P-printed specimens are subjected to direct impact tests to evaluate the material's impact strength. In the final stage, the identified voids and the results from the direct impact tests are correlated, allowing for a comprehensive understanding of how porosity relates to the impact strength of the 3D-printed specimens.

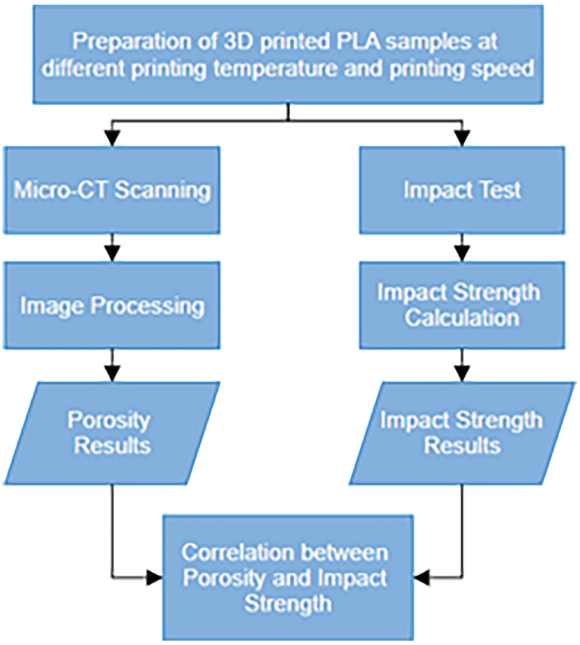

Figure 3: Flow chart of the experimental work

2.1 Preparation of Samples

An UltiMaker 2+ 3D Printer was utilized for the printing process. This printer has a build volume of 223 mm × 220 mm × 205 mm with a nozzle diameter of 0.4 mm, and a maximum nozzle temperature of 260°C. The material selected for the investigation was polylactic acid (PLA) (Ultimaker, Zaltbommel, The Netherlands), with a filament diameter of 2.85 mm. The PLA filament has tensile modulus of 3250 ± 119 MPa (XY-Flat), a flexural modulus of 3019 ± 87 MPa, and a Charpy impact strength of 3.9 ± 0.4 kJ/m^2 [33]. Other properties and the details of the manufacturer's test method/standard are available in the manufacturer's technical data sheet [33].

The Surface Tessellation Language (STL) file of 1 cm^3 cube sample and impact test samples, according to ASTM D6110-18 [34], were created using Autodesk Inventor 2024, as shown in Fig. 4. The print path code and other parameters were generated using the slicing software UltiMaker CURA 5.4.0.

The investigation focused solely on varying the printing temperature and printing speed to study their effects on porosity and mechanical strength, while keeping other processing parameters constant. The fixed parameters are outlined in Table 1. A layer height of 0.1 mm was selected to reduce the void [27,29]. A flat build orientation was selected to optimise the impact strength [35]. The build plate temperature was set

to 60°C, based on the recommended temperature range for PLA and our preliminary tests to obtain good first-layer adhesion. A raster angle of 45° was selected for optimal impact strength [36].

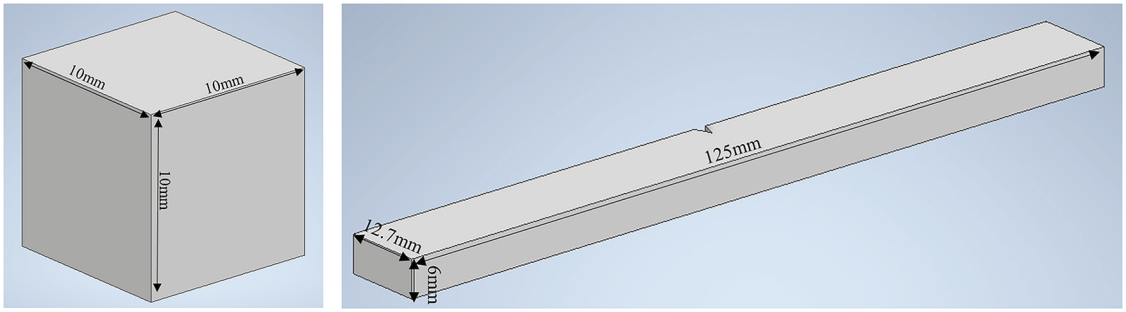

Figure 4: (**a**) $1 * 1 * 1\ cm^3$ samples for micro-CT analysis and (**b**) $125 * 12.7 * 6\ mm^3$ samples for ASTM D6110-18 impact test

Table 1: Fixed printing parameters

Parameter	Setting
Printing material	Polylactic Acid (PLA)
Layer height	0.1 mm
Build orientation	Flat
Infill density	100%
Infill pattern	Lines
Build plate temperature	60°C
Raster angle	45°

Based on the findings of a review study, the recommended extrusion temperature range for PLA parts falls between 180°C and 240°C [37]. At printing temperatures below 180°C, the PLA material does not fully reach its melting point [38]. The 3D printer utilized in this study has a default printing speed of 60 mm/s. Without altering any other printing parameters, the study commenced by exploring the minimum and maximum printing speeds achievable with this 3D printer. Hence, $1\ cm^3$ cube samples were printed at each printing temperature ranging from 180°C to 240°C at intervals of 20°C, and printing speeds ranging from 50 to 110 mm/s at intervals of 30 mm/s, as shown in Table 2.

Table 2: Printing parameters of cube (C1 to C12) and impact (D1 to D12) samples

Code	Printing speed (mm/s)	Printing temperature (°C)
C1, D1	50	180
C2, D2	80	180
C3, D3	110	180
C4, D4	50	200
C5, D5	80	200
C6, D6	110	200
C7, D7	50	220

(Continued)

Table 2 (continued)

Code	Printing speed (mm/s)	Printing temperature (°C)
C8, D8	80	220
C9, D9	110	220
C10, D10	50	240
C11, D11	80	240
C12, D12	110	240

2.2 MicroCT Image Acquisition and Processing

MicroCT images were acquired using a SkyScan 1172 (Kontich, Belgium) at the Malaysian Nuclear Agency based on scanning parameters in Table 3. Following acquisition, the raw data were reconstructed into high-resolution images (13.07 µm voxel size) using NRecon Software, V1.6.10.4.

Table 3: MicroCT scanning parameters

Scanner	SkyScan 1172
X-Ray Source voltage	40 kV
X-Ray Source power	10 W
X-Ray Source current	250 µA
Exposure	1573 ms
Rotation step	0.7°
Source-to-image distance	217.886 mm
Source-to-object distance	124.08 mm
Vertical object position	53 mm
Optical axis	510 lines
Camera	Hamamatsu 1.3 Mp camera
Camera pixel size	22.95 µm
Camera XY ratio	0.999
Image pixel size	13.07 µm

2.2.1 Computational Image Analysis

MicroCT images were analyzed using Python 3.8 libraries SimpleITK and scikit-image. First, noise in the images was reduced using a recursive Gaussian filter with a filter width of $\sigma = 0.2$ (Fig. 5a). Thereafter, the 3D-printed samples were segmented using Otsu's method [39] (Fig. 5b), and all pores were closed by applying a morphological closing operation with a kernel radius size of 20 voxels (Fig. 5c). To exclude regions where the outer wall intersects with the infill that could bias the porosity measurements, the masked images were eroded using an iterative process to a final erosion of 50 voxels (Fig. 5d). A masked image was then created multiplying the filtered image by the segmented one (Fig. 5e) and porosity within the sample was segmented using a moments threshold image filter [40] on the masked image (Fig. 5f). The volume of the printed sample and the volume of the pores were then measured, and porosity was determined. Finally, the average pore size was evaluated using the BoneJ plugin [41] in Fiji [42].

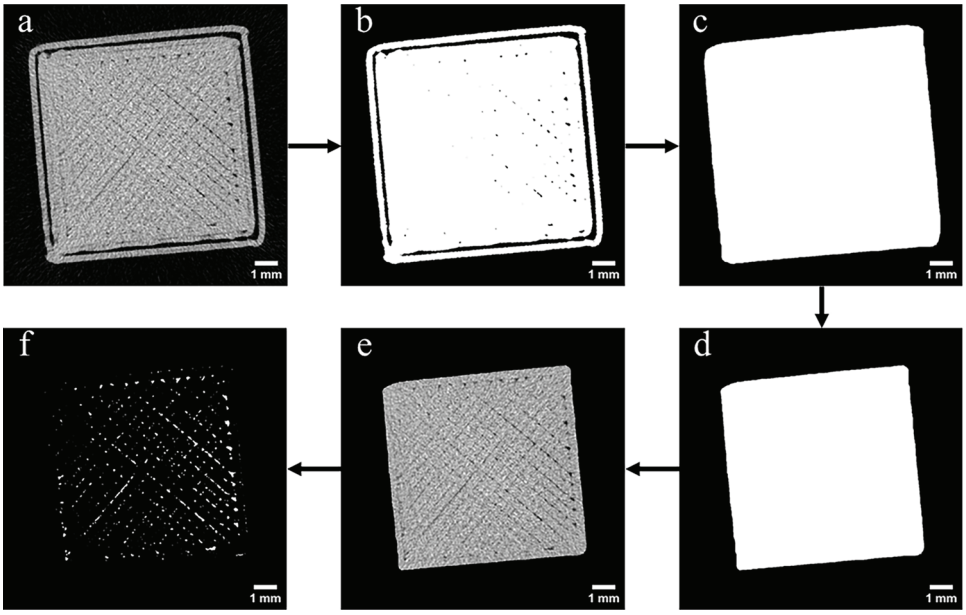

Figure 5: Segmentation of 3D printed sample's porosity. (**a**) Micro-CT image after noise filtering. (**b**) Segmented sample using Otsu's method. (**c**) Binary mask after morphological closing. (**d**) Eroded mask. (**e**) Volume of interest analyzed. (**f**) Porosity within the 3D printed sample

2.3 Direct Impact Test

The Charpy impact tests were performed using an impact tester machine (LY-XJL-22/50D Digital Impact Test Machine, Dongguan, China). Once the sample was positioned, the pendulum was raised to its initial position and securely fastened using the locking mechanism. The release energy and the speed were set in the digital display panel. Upon release, the pendulum traveled through the sample, causing it to fracture. The energy absorbed during this process was recorded from the digital display panel. This sequence was repeated for each sample to ensure consistent and reliable results. Charpy impact experiments for all the twelve sets, as reported in Table 2 were conducted and each impact test was repeated three times. The impact strength was calculated using Eq. (1) by dividing the energy absorbed, E (kJ), with the thickness, b (m), and the width of the sample, h (m) [43].

$$\textit{Impact Strength}\ (\mathrm{kJ/m^2}) = \frac{E}{b \cdot h} \tag{1}$$

3 Results and Discussions

3.1 Porosity Identification

MicroCT images allowed visualization and quantification of porosity within the printed PLA samples in 3D (Fig. 6).

Table 4 provides a summary of the porosity details for the different samples, indicating how variations in printing temperature and printing speed impact porosity. The influence of the printing temperature on the porosity of printed PLA can be seen in Fig. 7. In general, the mean pore size decreased as the printing temperature increased from 180°C to 220°C, except at 50 mm/s. At 50 mm/s, the mean pore size decreased by 29.8% when the printing temperature increased from 180°C to 240°C, whereas at 80 and 110 mm/s, maximum reductions of 22.6% and 36.8% in mean pore size were obtained at 220°C. Beyond 220°C, the mean pore

size increased. Similar observations were reported by Charlon et al. [19], where the porosity of MEX-printed polypropylene was reduced with the increase in printing temperature from 170°C to 180°C.

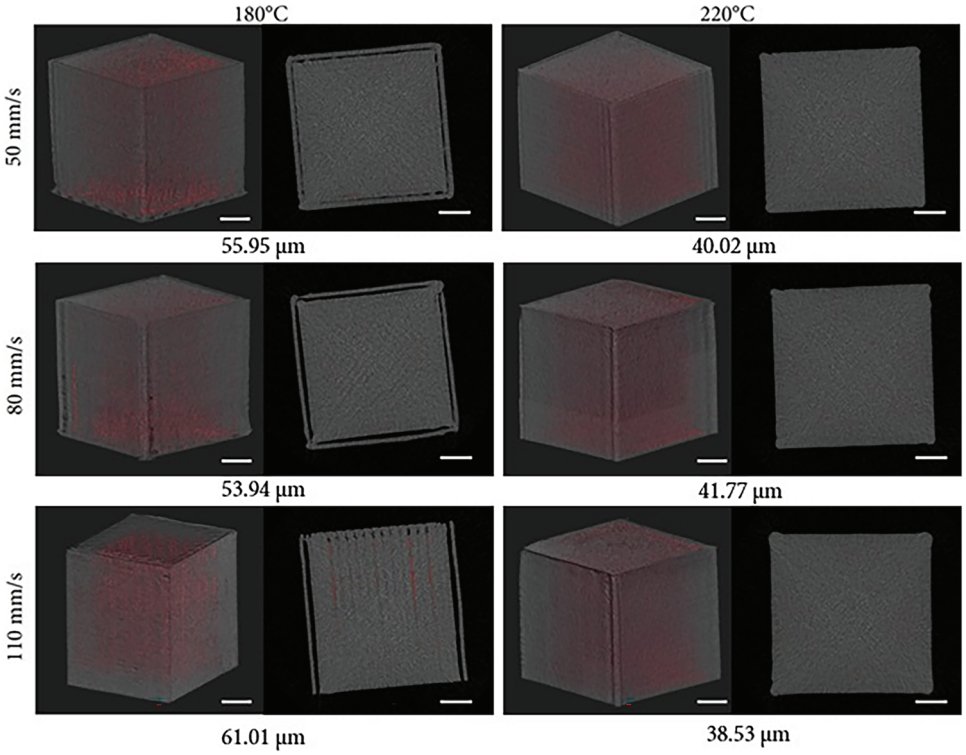

Figure 6: MicroCT images of PLA samples printed at 180°C and 220°C at increasing printing speeds (50, 80, and 110 mm/s). 3D visualization of the samples and representative cross-section are shown, with pore volume overlaid in red colour onto original images. Mean Pore Size (µm) is reported at the bottom of each sample. Please note porosity is represented for the analysed volume of interest as described in Section 2.2.1. Scale bars correspond to 2 mm

Table 4: Porosity details of the PLA samples

Code	Printing speed (mm/s)	Printing temperature (°C)	Mean pore size (µm)	Porosity percentage (%)
C1	50	180	55.95	1.67
C2	80	180	53.94	1.58
C3	110	180	61.01	2.58
C4	50	200	43.16	2.41
C5	80	200	47.51	1.71
C6	110	200	39.38	1.86
C7	50	220	40.02	1.99
C8	80	220	41.77	2.08
C9	110	220	38.53	2.28
C10	50	240	39.26	2.33
C11	80	240	55.15	2.50
C12	110	240	40.70	2.00

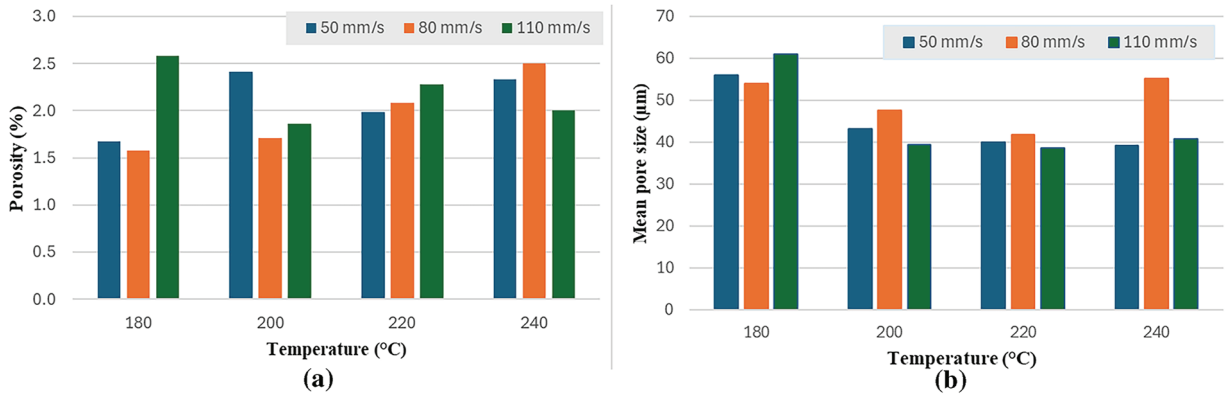

Figure 7: (**a**) Porosity and (**b**) mean pore size as a function of printing temperature

The highest percentage porosity was obtained at the lowest temperature and highest printing speed (180°C at 110 mm/s). As reported previously, the absorbed moisture in the PLA filament evaporated as steam during printing and created bubbles/voids in the MEX-manufactured part, and the porosity in the 3D-printed PLA is proportional to the storage relative humidity [44]. PLA absorbs water molecules when exposed to the ambient environment. When the printing temperature increases, the absorbed water in the PLA filament vaporizes into steam, leading to the formation of more bubbles/voids within the fabricated part. Furthermore, elevating the printing temperature raises the temperature of the molten material, resulting in a decrease in viscosity. The increase in printing temperature enhances the mobility of PLA polymer chains, facilitating the fusion between the layers [19]. The lower viscosity prevents the bubbles from coalescing into larger pores. As a result, although more voids were formed but they are smaller in mean pore size due to the higher viscosity of PLA, as observed in the current work.

In MEX/TRB-P 3D printing, bonding between filament layers can be categorized as in-layer and inter-layer bonding. In-layer bonding occurs between adjacent filaments within the same layer, while inter-layer bonding occurs between successive layers. As the melt is extruded from the nozzle, it undergoes convective cooling from the environment and conductive cooling from the previous layer [45]. The results obtained for printed PLA at a lower printing temperature in Fig. 7b are likely due to reduced adhesion between deposited filaments and layers [46], a similar observation was reported by Morales et al. [47]. Higher printing temperatures reduce interlayer voids by enhancing material fluidity, improving interaction between material chains, and decreasing discontinuities, thereby contributing to a denser and more structurally sound 3D-printed object, which reduces the inter-layer voids and thus reduces the mean pore size. Lower printing temperatures may lead to poor layer-to-layer bonding and increased void size due to incomplete melting of the material [48]. Furthermore, the printed PLA may not melt sufficiently to achieve the optimum viscosity, resulting in weak bonding between neighboring particles and layers [49].

The influence of the printing speed on the porosity of printed PLA can be seen in Fig. 8. As reported previously, the highest percentage of porosity was obtained at the highest printing speed (of 110 mm/s) and the lowest printing temperature (of 180°C). A similar trend was observed in previous work, where increasing the printing speed during MEX 3D printing reduced voids between beads [16]. Based on Fig. 8, the mean pore size initially increased with the increasing printing speed due to under-extrusion, where thermal shrinkage has occurred during the cooling of materials [50]. In general, the mean pore size increased with printing speed, until a certain point, beyond which it decreased. Similar results were reported previously, where a slower printing speed resulted in more contact between adjacent roads [13], and as such higher printing speed resulted in larger pores. In addition to the effects of interlayer adhesion and material compaction

during the MEX printing process, printing speed also plays an important role in determining the density of MEX-fabricated parts. At lower printing speeds, the semi-molten polymer extruded from the nozzle has more time to spread and flow into the adjacent gaps and inter-filament voids before the semi-molten polymer solidifies. The improved wetting and filling behavior reduces the presence of porosity and micro-voids between deposited filaments. Consequently, components printed at lower speeds typically exhibit higher density and reduced porosity compared to those manufactured at higher printing speeds. As a result, the insufficient spreading and rapid solidification of the semi-molten polymer limit the chance of interfacial contact and void closure [51]. Therefore, lower printing speeds allow for better bonding between layers and provide sufficient time for material fusion.

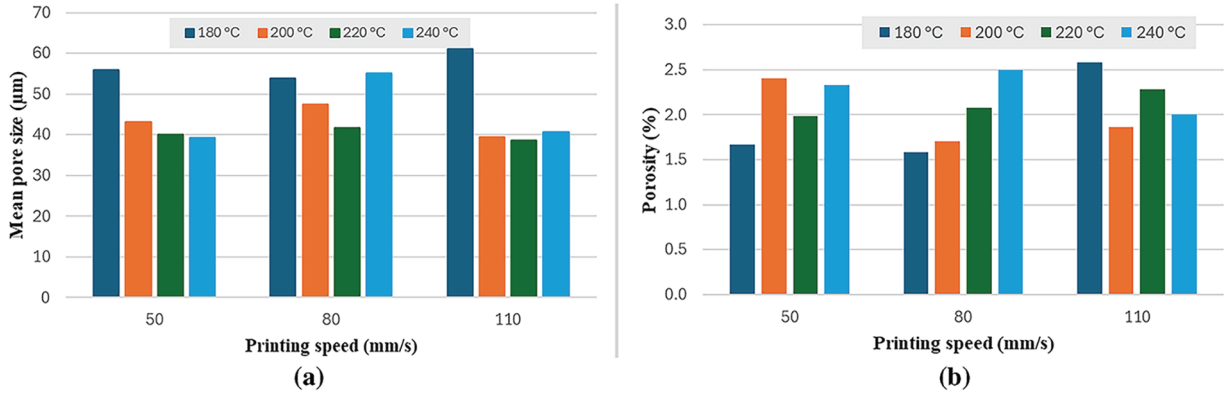

Figure 8: (**a**) Porosity and (**b**) mean pore size as a function of printing speed

In contrast, higher printing speeds reduce extrusion volume and printing stability, which leads to rough fractured sections with substantial voids [52]. Furthermore, the volumetric flow rate from the nozzle does not scale linearly with printing speed [53]. Consequently, as printing speed increases, there is a reduced supply of materials through the nozzle, resulting in thinner extruded paths. As the printing speed increases, the complete extrusion of the material transpires before the onset of the thermal decomposition reaction initiated by the nozzle temperature [54].

3.2 Charpy Impact Strength

Table 5 provides the calculated average Charpy impact strength for the 3 printed PLA specimens at different printing temperatures and printing speeds, indicating the variations in printing parameters on impact strength. The results are illustrated in the graphs shown in Fig. 9.

Fig. 9a shows the impact of increasing printing speed from 50 to 110 mm/s on Charpy impact strength at print temperatures of 180°C, 200°C, 220°C, and 240°C. Generally, as the printing speed increases, the impact strength of printed PLA decreases, except for the specimen printed at 240°C. Higher printing speed results in poor layer bonding performance due to the rapid cooling of the plastic, which results in insufficient temperature being applied to the extruded layer and poor adhesion to the layer underneath [55]. Hence, selecting a high printing speed can cause inadequate layer bonding, consequently diminishing the mechanical strength of the part [49].

However, when the printing temperature is excessively high at a low printing speed, the viscosity of the molten PLA decreases significantly. This reduced viscosity of molten PLA affects the dimensional stability of the deposited material. The low viscosity semi-molten PLA filament is subjected to undesired deformation such as spreading, sagging, or distortion before the semi-molten PLA fully solidify. Furthermore, a higher

printing temperature increases the cooling and solidification time required for each deposited PLA layer, which may produce warping, deformation, and eventually affect the geometrical accuracy in the final component. On the other hand, at a printing temperature of 240°C, the impact strength of the manufactured parts increases with higher printing speeds. This improvement is likely contributed by a more balanced interaction between the flow of the molten PLA, solidification rate, and interlayer bonding, which reduces excessive heat accumulation while still maintaining adequate interlayer adhesion [49]. If the set temperature is too low at high speeds, the filament may not melt at a sufficient rate, leading to material getting stuck inside the nozzle and resulting in a higher viscosity melt than desired. Therefore, it can be concluded that the printing temperature and printing speed should be appropriately matched, where increasing the printing speed should also necessitate an increase in printing temperature to ensure the filament is fully melted before being deposited [49].

Table 5: Charpy impact strength results

Code	Printing speed (mm/s)	Printing temperature (°C)	Impact strength (kJ/m^2)
D01	50	180	78.65 ± 18.6
D02	80	180	64.86 ± 1.2
D03	110	180	38.21 ± 6.9
D04	50	200	97.88 ± 6.3
D05	80	200	81.18 ± 2.8
D06	110	200	57.15 ± 12.2
D07	50	220	120.92 ± 7.5
D08	80	220	101.77 ± 2.5
D09	110	220	81.89 ± 10.1
D10	50	240	72.43 ± 23.5
D11	80	240	84.87 ± 44.5
D12	110	240	98.68 ± 17.9

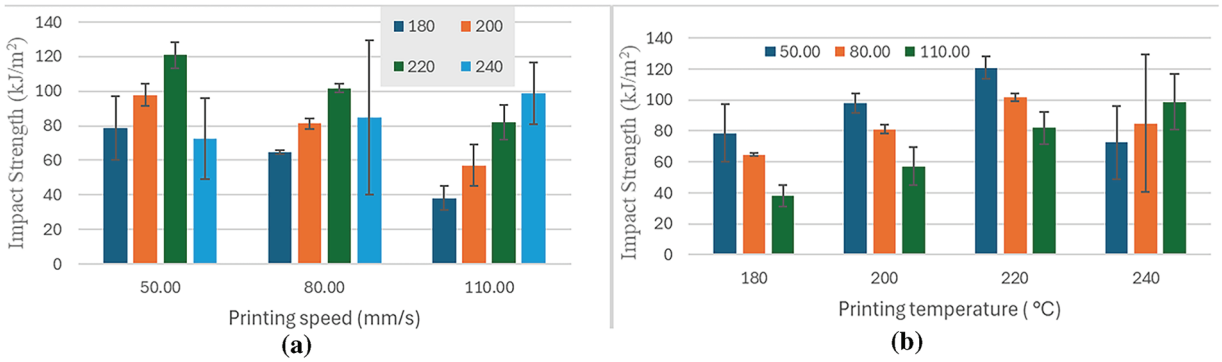

Figure 9: Charpy Impact strength of printed PLA specimens as a function of (**a**) printing speed (**b**) printing temperature

Fig. 9b illustrates the impact of increasing printing temperature from 180°C to 240°C on porosity at print speeds of 50, 80, and 110 mm/s. As the printing temperature increases from 180°C to 220°C, the impact strength of printed PLA increases. At 220°C, improvements in impact strength of 53.7%, 56.9%, and 114% were observed for samples printed at 50, 80, and 110 mm/s, respectively. After 220°C, the impact strengths for

the samples printed at 50 and 80 mm/s were then reduced. At lower temperature, PLA polymer chains lack the necessary mobility to effectively diffuse across the interface [19]. At higher printing temperatures, the increased flow of melted resin from the printer nozzle leads to greater deviation, attributable to the decrease in shear viscosity [56]. Increasing the printing temperature led to stronger thermal bonding and stronger interlayer lamination, resulting in increased mechanical properties [22,57]. However, as the temperature of the nozzle rises, there is a promotion of reptation and entanglement among the polymer chains at the interface due to an increase in chain diffusion. Therefore, the impact strength of printed PLA was reduced after 220°C. Increasing the printing temperature has a significant impact on the viscosity of molten PLA. As the nozzle temperature rises, the viscosity of the molten PLA decreases. Consequently, this temperature-dependent behavior facilitates better diffusion of newly extruded PLA molecules into the underlying layer, which enhances the interlayer adhesion strength of the printed material [20]. Regarding adhesion strength, Sun et al. [46] and Sood et al. [58] suggest that increasing the printing temperature enhances the adhesion between layers. Fernandes et al. [59] observed that increasing printing temperature enhances the contact area between layers because the extruded material becomes oval from a circular shape as viscosity decreases with the rising printing temperature.

Higher printing temperatures during MEX/TRB-P resulted in increased crystallinity due to the reheating of previously deposited layers as new filaments were extruded [60]. The increase in PLA crystallinity correlates with changes in its mechanical properties, where an increase in the crystallinity of 3D-printed PLA corresponded to higher impact strength [61,62]. Hence, it can be concluded that the results depicted in Fig. 9, where printing temperature increases correspond to higher impact strength, are partially due to the increasing crystallinity.

3.3 Correlation between Porosity and Charpy Impact Strength

The relationship between impact strength and mean pore size at different printing temperatures and printing speeds can be obtained from Fig. 10a,b. In general, the impact strength decreases as the mean pore size increases, as shown in Fig. 10c, except for the results at a printing temperature of 240°C. Several researchers observed the same effect of porosity on mechanical properties [8,63,64]. The voids in the printed PLA are the primary causes of the impact strength reduction observed in Fig. 8. Voids serve as stress concentration points within the printed PLA, facilitating the initiation of cracks that propagate to the nearby regions. Porosity is distributed at critical locations, and when load is applied, interlaminar cracks rapidly propagate due to the high interlayer porosity, leading to the separation of printed layers [6]. Tao et al. [65] stated that reducing the porosity of the cross-section led to increased density and enhanced force-bearing capacity of the part. Higher porosity diminishes the effective cross-sectional area of the material available to resist the applied load during impact. The impact strength of printed PLA decreases due to the presence of voids, as the material's capacity to absorb impact energy is compromised [66].

At low printing temperatures, the printed PLA with low fluidity and high viscosity leads to inadequate bonding and increased porosity between the lines and layers of the molten polymer, which results in poor impact strength [67]. Conversely, with an increase in printing temperature, the viscosity of printed PLA decreases, which results in decreased mean pore size and therefore increased impact strength. When the printing speed increases, the porosity increases, while the impact strength decreases. This is because at high printing speed, rapid heat dissipation causes insufficient melting rate and reduces the fusion between layers [38]. Therefore, at a high printing temperature (220°C) and low printing speed (50 mm/s), the porosity of the printed PLA is reduced, and the impact strength is increased.

The results at printing temperatures of 180°C, 200°C, and 220°C are aligned with the trend of previous works. However, the results for a printing temperature of 240°C deviate from the trends observed, which

show unpredictable and inconsistent results. There was a big range between the highest and lowest impact strength in the 240°C printed specimens. Tian et al. [68] corroborated this finding through experiments that PLA transitions into a liquid state at temperatures above 240°C, leading to uncontrolled flow from the nozzle and compromising printing precision. Printing PLA above its degradation temperature results in the material becoming increasingly brittle and less ductile over time [69]. Hence, the material tends to have lower viscosity, prolonging the cooling time, which can impact the degree of crystallinity. Additionally, at a very high printing temperature, adjacent particles and layers may be deposited before adequate cooling, affecting bonding between layers, which results in challenges in maintaining the dimensional stability of the printed part [49]. Similarly, Khosravani and Reinicke [70] suggested that thermal degradation within the extruder leads to the generation of gas, resulting in the formation of numerous trapped bubbles within the filament. This phenomenon may appear as a noticeable foaming effect. The upper layer of material fails to fully cool after melting when the printing temperature is excessively high, which introduces defects during the forming process. These defects diminish the mechanical properties of the sample.

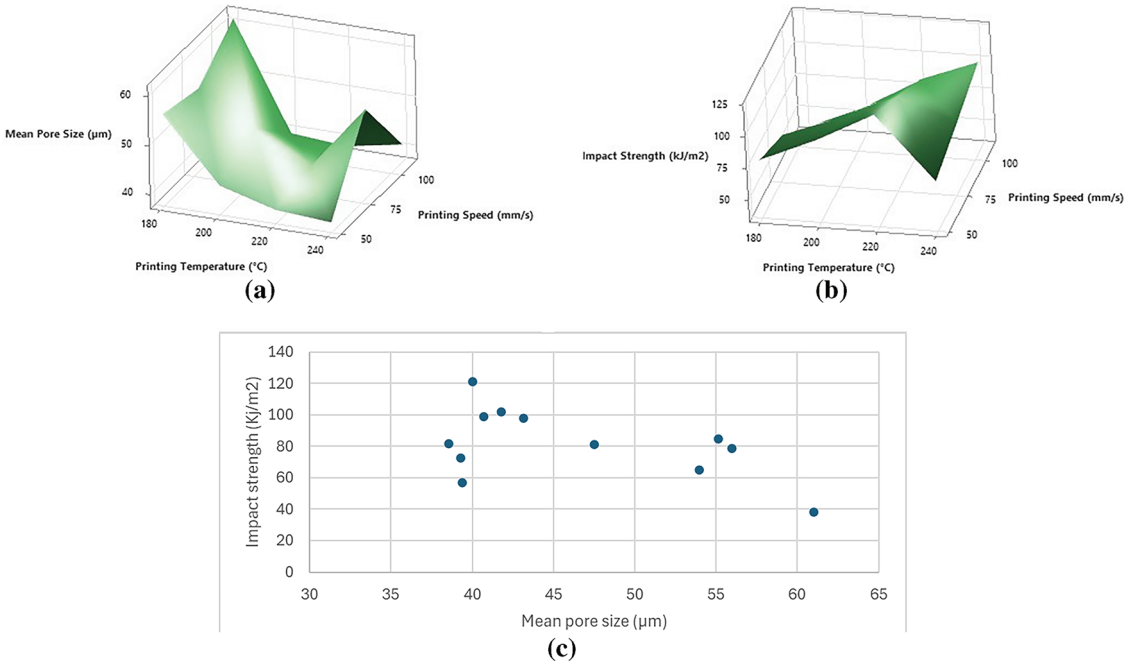

Figure 10: (**a**) Porosity and (**b**) impact strength against printing temperature and printing speed, (**c**) Correlation between impact strength (kJ/m^2) and mean pore size (µm)

4 Conclusions

In the present work, the effects of printing temperature and printing speed on the porosity and impact strength of material extrusion 3D printed PLA along with the relationship between porosity and Charpy impact strength, have been identified. MicroCT imaging and impact tests were conducted where the PLA specimens were printed at printing speeds ranging from 50 to 110 mm/s and printing temperatures ranging from 180°C to 220°C. Current work has led to the following conclusions:

- The printing temperature of 220°C and printing speed of 50 mm/s yielded the best impact behavior and a smaller mean pore size.
- Increasing the printing temperature caused the mean pore size of the printed PLA to decrease due to enhanced material fluidity and improved interaction between material chains.

- The same effect was observed when the print speed was decreased, where a low printing temperature allows enough time for material fusion.
- Increasing the printing temperature and decreasing the printing speed increases the impact strength due to better thermal bonding and enhanced interlayer adhesion strength.
- The impact strength decreases as the porosity increases. Higher porosity decreases the effective cross-sectional area of the material available to resist the applied load during impact.
- Results at 240°C are different from expectations due to material degradation and overheating, which introduce defects during the material deposition process.

Acknowledgement: The first author wishes to express his sincere appreciation to Heriot-Watt University Malaysia and the Malaysian Nuclear Agency for providing research support and essential laboratory equipment, which significantly contributed to the success of this study.

Funding Statement: The authors received no specific funding for this study.

Author Contributions: The authors confirm contribution to the paper as follows: Conceptualization, Tze Chuen Yap; methodology, Jia Yan Lim and Tze Chuen Yap; validation, Siti Madiha Muhammad Amir and Tze Chuen Yap; formal analysis, Jia Yan Lim and Tze Chuen Yap; investigation, Jia Yan Lim, Roslan Yahya and Marta Peña Fernández; resources, Siti Madiha Muhammad Amir and Tze Chuen Yap; data curation, Jia Yan Lim and Tze Chuen Yap; writing—original draft preparation, Jia Yan Lim and Tze Chuen Yap; writing—review and editing, Tze Chuen Yap, Marta Peña Fernández, Siti Madiha Muhammad Amir and Roslan Yahya; visualization, Jia Yan Lim, Marta Peña Fernández and Tze Chuen Yap; supervision, Siti Madiha Muhammad Amir and Tze Chuen Yap; project administration, Tze Chuen Yap. All authors reviewed the results and approved the final version of the manuscript.

Availability of Data and Materials: The data that support the findings of this study are available from the corresponding author, Tze Chuen Yap, upon reasonable request.

Ethics Approval: Not applicable.

Conflicts of Interest: The authors declare no conflicts of interest to report regarding the present study.

References

1. Gibson I, Rosen D, Stucker B. Additive manufacturing technologies: 3D printing, rapid prototyping, and direct digital manufacturing. 2nd ed. New York, NY, USA: Springer; 2015. 498 p.
2. Mwema FM, Akinlabi ET. Basics of fused deposition modelling (FDM). In: Fused deposition modeling: strategies for quality enhancement. Cham, Switzerland: Springer International Publishing; 2020. p. 1–15.
3. Menezes PL, Misra M, Kumar P. Tribology of additively manufactured materials: fundamentals, modeling, and applications. Amsterdam, The Netherlands: Elsevier; 2022. 360 p.
4. Tao Y, Kong F, Li Z, Zhang J, Zhao X, Yin Q, et al. A review on voids of 3D printed parts by fused filament fabrication. J Mater Res Technol. 2021;15:4860–79. doi:10.1016/j.jmrt.2021.10.108.
5. Al-Maharma AY, Patil SP, Markert B. Effects of porosity on the mechanical properties of additively manufactured components: a critical review. Mater Res Express. 2020;7(12):122001. doi:10.1088/2053-1591/abcc5d.
6. Tronvoll SA, Welo T, Elverum CW. The effects of voids on structural properties of fused deposition modelled parts: a probabilistic approach. Int J Adv Manuf Technol. 2018;97(9–12):3607–18. doi:10.1007/s00170-018-2148-x.
7. Perkins A, Yang W, Liu Y, Chen L, Yenusah C. Finite element analysis of the effect of porosity on the plasticity and damage behavior of Mg AZ31 and Al 6061 T651 alloys. ASME Int Mech Eng Congr Expo. 2020;9:9. doi:10.1115/IMECE2019-10672.
8. Wang X, Zhao L, Fuh JYH, Lee HP. Effect of porosity on mechanical properties of 3D printed polymers: experiments and micromechanical modeling based on X-ray computed tomography analysis. Polymers. 2019;11(7):1154. doi:10.3390/polym11071154.

9. Muzli MF, Ismail KI, Yap TC. Effects of infill density and printing speed on the tensile behaviour of fused deposition modelling 3D printed PLA specimens. J Eng Technol Appl Phys. 2024;6(2):1–8.
10. Amirruddin MS, Ismail KI, Yap TC. Effect of layer thickness and raster angle on the tribological behavior of 3D printed materials. Mater Today Proc. 2022;48:1821–5. doi:10.1016/j.matpr.2021.09.139.
11. von Windheim N, Collinson DW, Lau T, Brinson LC, Gall K. The influence of porosity, crystallinity and interlayer adhesion on the tensile strength of 3D printed polylactic acid (PLA). Rapid Prototyp J. 2021;27(7):1327–36. doi:10.1108/rpj-08-2020-0205.
12. Sun X, Mazur M, Cheng CT. A review of void reduction strategies in material extrusion-based additive manufacturing. Addit Manuf. 2023;67:103463. doi:10.1016/j.addma.2023.103463.
13. Abbott AC, Tandon GP, Bradford RL, Koerner H, Baur JW. Process-structure-property effects on ABS bond strength in fused filament fabrication. Addit Manuf. 2018;19:29–38. doi:10.1016/j.addma.2017.11.002.
14. Fan C, Shan Z, Zou G, Zhan L, Yan D. Interfacial bonding mechanism and mechanical performance of continuous fiber reinforced composites in additive manufacturing. Chin J Mech. 2021;34(1):21. doi:10.1186/s10033-021-00538-7.
15. Miazio L. Impact of print speed on strength of samples printed in FDM technology. Agric Eng. 2019;23(2):33–8. doi:10.1515/agriceng-2019-0014.
16. Abualbandora TA, Alshneeqat MG, Mourad AHI. Impact of 3D printing parameters of short carbon fiber reinforced polymer CFRP on the mechanical and failure performance: review and future perspective. Next Mater. 2025;8:100645. doi:10.1016/j.nxmate.2025.100645.
17. Natarajan SM, Senthil S, Narayanasamy P. Investigation of mechanical properties of FDM-processed *Acacia concinna*–filled polylactic acid filament. Int J Polym Sci. 2022;2022:4761481. doi:10.1155/2022/4761481.
18. Pang R, Lai MK, Ismail KI, Yap TC. Characterization of the dimensional precision, physical bonding, and tensile performance of 3D-printed PLA parts with different printing temperature. J Manuf Mater Process. 2024;8(2):56. doi:10.3390/jmmp8020056.
19. Charlon S, Le Boterff J, Soulestin J. Fused filament fabrication of polypropylene: influence of the bead temperature on adhesion and porosity. Addit Manuf. 2021;38:101838. doi:10.1016/j.addma.2021.101838.
20. Behzadnasab M, Yousefi A. Effects of 3D printer nozzle head temperature on the physical and mechanical properties of PLA based product. In: 12th International Seminar on Polymer Science and Technology (ISPST); 2016 Nov 2–5; Tehran, Iran: Islamic Azad University; 2016. p. 3–5.
21. Zainal MA, Ismail KI, Yap TC. Tribological properties of PLA 3D printed at different extrusion temperature. J Phys Conf Ser. 2023;2542(1):012001. doi:10.1088/1742-6596/2542/1/012001.
22. Pang R, Lai MK, Teo HH, Yap TC. Influence of temperature on interlayer adhesion and structural integrity in material extrusion: a comprehensive review. J Manuf Mater Process. 2025;9:196. doi:10.3390/jmmp9060196.
23. Sultana J, Rahman MM, Wang Y, Ahmed A, Xiaohu C. Influences of 3D printing parameters on the mechanical properties of wood PLA filament: an experimental analysis by Taguchi method. Prog Addit Manuf. 2024;9(4):1239–51. doi:10.1007/s40964-023-00516-6.
24. Aqida SN, Ghazali MI, Hashim J. Effect of porosity on mechanical properties of metal matrix composite: an overview. J Teknol. 2004;40:17. doi:10.11113/jt.v40.395.
25. Shelmerdine SC, Simcock IC, Hutchinson JC, Aughwane R, Melbourne A, Nikitichev DI, et al. 3D printing from microfocus computed tomography (micro-CT) in human specimens: education and future implications. Br J Radiol. 2018;91(1088):20180306. doi:10.1259/bjr.20180306.
26. Du Plessis A, Yadroitsev I, Yadroitsava I, Le Roux SG. X-Ray microcomputed tomography in additive manufacturing: a review of the current technology and applications. 3D Print Addit Manuf. 2018;5(3):227–47. doi:10.1089/3dp.2018.0060.
27. Vidakis N, David C, Petousis M, Sagris D, Mountakis N, Moutsopoulou A. The effect of six key process control parameters on the surface roughness, dimensional accuracy, and porosity in material extrusion 3D printing of polylactic acid: prediction models and optimization supported by robust design analysis. Adv Ind Manuf Eng. 2022;5:100104. doi:10.1016/j.aime.2022.100104.

28. Vidakis N, David C, Petousis M, Sagris D, Mountakis N. Optimization of key quality indicators in material extrusion 3D printing of acrylonitrile butadiene styrene: the impact of critical process control parameters on the surface roughness, dimensional accuracy, and porosity. Mater Today Commun. 2023;34:105171. doi:10.1016/j.mtcomm.2022.105171.
29. Faizaan M, Shenoy BS, Nunna S, Mallya R, Rao US, Ramanath KC, et al. A study on the overall variance and void architecture on MEX-PLA tensile properties through printing parameter optimisation. Sci Rep. 2025;15(1):1–12. doi:10.1038/s41598-025-87348-2.
30. Petousis M, Michailidis N, Kulas V, Papadakis V, Spiridaki M, Mountakis N, et al. Sustainability-driven additive manufacturing: implementation and content optimization of fine powder recycled glass in polylactic acid for material extrusion 3D printing. Int J Lightweight Mater Manuf. 2025;8(5):595–610. doi:10.1016/j.ijlmm.2025.02.008.
31. Vidakis N, Kalderis D, Michailidis N, Papadakis V, Mountakis N, Argyros A, et al. Environmentally friendly polylactic acid/ferronickel slag composite filaments for material extrusion 3D printing: a comprehensive optimization of the filler content. Mater Today Sustain. 2024;27:100881. doi:10.1016/j.mtsust.2024.100881.
32. Wu H, Chen X, Xu S, Zhao T. Evolution of manufacturing defects of 3D-printed thermoplastic composites with processing parameters: a Micro-CT analysis. Materials. 2023;16:6521. doi:10.3390/ma16196521.
33. Ultimaker. Technical Data Sheet: Ultimaker PLA [Internet]. Utrecht, The Netherlands: Ultimaker B.V; 2018 [cited 2025 May 1]. Available from: https://support.ultimaker.com/hc/en-us/articles/360011962720-Ultimaker-PLA-TDS.
34. ASTM D6110-18. Standard test method for determining the Charpy impact resistance of notched specimens of plastics. West Conshohocken, PA, USA: ASTM International; 2018.
35. Huang B, Meng S, He H, Jia Y, Xu Y, Huang H. Study of processing parameters in fused deposition modeling based on mechanical properties of acrylonitrile-butadiene-styrene filament. Polym Eng Sci. 2019;59(1):120–8. doi:10.1002/pen.24875.
36. Dziewit P, Rajkowski K, Płatek P. Effects of building orientation and raster angle on the mechanical properties of selected materials used in FFF techniques. Materials. 2024;17:6076. doi:10.3390/ma17246076.
37. Zharylkassyn B, Perveen A, Talamona D. Effect of process parameters and materials on the dimensional accuracy of FDM parts. Mater Today Proc. 2021;44:1307–11. doi:10.1016/j.matpr.2020.11.332.
38. Hsueh MH, Lai CJ, Wang SH, Zeng YS, Hsieh CH, Pan CY, et al. Effect of printing parameters on the thermal and mechanical properties of 3D-printed PLA and PETG, using fused deposition modeling. Polymers. 2021;13:1758. doi:10.3390/polym13111758.
39. Otsu N. A threshold selection method from gray-level histograms. Trans Syst Man Cybern. 1979;9(1):62–6. doi:10.1109/TSMC.1979.4310076.
40. Tsai WH. Moment-preserving thresholding: a new approach. Comput Vis Graph Image Process. 1985;29(3):377–93. doi:10.1016/0734-189X(85)90133-1.
41. Doube M, Klosowski MM, Arganda-Carreras I, Cordelières FP, Dougherty RP, Jackson JS, et al. BoneJ: free and extensible bone image analysis in ImageJ. Bone. 2010;47(6):1076–9. doi:10.1016/j.bone.2010.08.023.
42. Schindelin J, Arganda-Carreras I, Frise E, Kaynig V, Longair M, Pietzsch T, et al. Fiji: an open-source platform for biological-image analysis. Nat Methods. 2012;9(7):676–82. doi:10.1038/nmeth.2019.
43. Tunçel O. Optimization of charpy impact strength of tough PLA samples produced by 3D printing using the taguchi method. Polymers. 2024;16:459. doi:10.3390/polym16040459.
44. Lendvai L, Fekete I, Jakab SK, Szarka G, Verebélyi K, Iván B. Influence of environmental humidity during filament storage on the structural and mechanical properties of material extrusion 3D-printed poly(lactic acid) parts. Results Eng. 2024;24:103013. doi:10.1016/j.rineng.2024.103013.
45. Lepoivre A, Boyard N, Levy A, Sobotka V. Heat transfer and adhesion study for the FFF additive manufacturing process. Procedia Manuf. 2020;47:948–55. doi:10.1016/j.promfg.2020.04.291.
46. Sun Q, Rizvi GM, Bellehumeur CT, Gu P. Effect of processing conditions on the bonding quality of FDM polymer filaments. Rapid Prototyp J. 2008;14(2):72–80. doi:10.1108/13552540810862028.

47. Morales NG, Fleck TJ, Rhoads JF. The effect of interlayer cooling on the mechanical properties of components printed via fused deposition. Addit Manuf. 2018;24:243–8. doi:10.1016/j.addma.2018.09.001.
48. Hsueh MH, Lai CJ, Liu KY, Chung CF, Wang SH, Pan CY, et al. Effects of printing temperature and filling percentage on the mechanical behavior of fused deposition molding technology components for 3D printing. Polymers. 2021;13:2910. doi:10.3390/polym13172910.
49. Abeykoon C, Sri-Amphorn P, Fernando A. Optimization of fused deposition modeling parameters for improved PLA and ABS 3D printed structures. Int J Lightweight Mater Manuf. 2020;3(3):284–97. doi:10.1016/j.ijlmm.2020.03.003.
50. Algarni M, Ghazali S. Comparative study of the sensitivity of PLA, ABS, PEEK, and PETG's mechanical properties to FDM printing process parameters. Crystals. 2021;11:995. doi:10.3390/cryst11080995.
51. Cardoso PHM, Coutinho RRTP, Drummond FR, da Conceição MN, Thiré RMSM. Evaluation of printing parameters on porosity and mechanical properties of 3D printed PLA/PBAT blend parts. Macromol Symp. 2020;394(1):2000157. doi:10.1002/masy.202000157.
52. Tegegne WW. Effect of voids and printing parameters on the mechanical behavior of composite structure manufactured by 3D printing fused deposition modeling [master's thesis]. Changsha, China: Central South University; 2021.
53. Loskot J, Jezbera D, Loskot R, Bušovský D, Barylski A, Glowka K, et al. Influence of print speed on the microstructure, morphology, and mechanical properties of 3D-printed PETG products. Polym Test. 2023;123:108055. doi:10.1016/j.polymertesting.2023.108055.
54. Yoo CJ, Shin BS, Kang BS, Yun DH, You DB, Hong SM. Manufacturing a porous structure according to the process parameters of functional 3D porous polymer printing technology based on a chemical blowing agent. IOP Conf Ser Mater Sci Eng. 2017;229(1):012027.
55. Johansson F. Optimizing fused filament fabrication 3D printing for durability: tensile properties and layer bonding. Blekinge Inst Technol. 2016;26:952.
56. Akbaş OE, Hıra O, Hervan SZ, Samankan S, Altınkaynak A. Dimensional accuracy of FDM-printed polymer parts. Rapid Prototyp J. 2020;26(2):288–98. doi:10.1108/rpj-04-2019-0115.
57. Tymrak BM, Kreiger M, Pearce JM. Mechanical properties of components fabricated with open-source 3-D printers under realistic environmental conditions. Mater Des. 2014;58:242–6. doi:10.1016/j.matdes.2014.02.038.
58. Sood AK, Ohdar RK, Mahapatra SS. Experimental investigation and empirical modelling of FDM process for compressive strength improvement. J Adv Res. 2012;3(1):81–90. doi:10.1016/j.jare.2011.05.001.
59. Fernandes J, Deus AM, Reis L, Vaz MF, Leite M. Study of the influence of 3D printing parameters on the mechanical properties of PLA. In: Proceedings of the International Conference on Progress in Additive Manufacturing; 2018 May 14–17. Singapore.
60. Drummer D, Cifuentes-Cuéllar S, Rietzel D. Suitability of PLA/TCP for fused deposition modeling. Rapid Prototyp J. 2012;18(6):500–7. doi:10.1108/13552541211272045.
61. Benwood C, Anstey A, Andrzejewski J, Misra M, Mohanty AK. Improving the impact strength and heat resistance of 3D printed models: structure, property, and processing correlationships during fused deposition modeling (FDM) of poly(lactic acid). ACS Omega. 2018;3(4):4400–11. doi:10.1021/acsomega.8b00129.
62. Wang L, Gramlich WM, Gardner DJ. Improving the impact strength of poly(lactic acid) (PLA) in fused layer modeling (FLM). Polymer. 2017;114:242–8. doi:10.1016/j.polymer.2017.03.011.
63. Ning F, Cong W, Qiu J, Wei J, Wang S. Additive manufacturing of carbon fiber reinforced thermoplastic composites using fused deposition modeling. Compos B Eng. 2015;80:369–78. doi:10.1016/j.compositesb.2015.06.013.
64. Guo Y, Chen C, Wang Q, Liu M, Cao Y, Pan Y, et al. Effect of porosity on mechanical properties of porous tantalum scaffolds produced by electron beam powder bed fusion. Trans Nonferrous Met Soc China. 2022;32(9):2922–34. doi:10.1016/s1003-6326(22)65993-4.
65. Tao Y, Li P, Pan L. Improving tensile properties of polylactic acid parts by adjusting printing parameters of open source 3D printers. Mater Sci. 2020;26(1):83–7. doi:10.5755/j01.ms.26.1.20952.

66. Kumar KR, Mohanavel V, Kiran K. Mechanical properties and characterization of polylactic acid/carbon fiber composite fabricated by fused deposition modeling. J Mater Eng Perform. 2022;31(6):4877–86. doi:10.1007/s11665-021-06566-7.
67. Valerga AP, Batista M, Salguero J, Girot F. Influence of PLA filament conditions on characteristics of FDM parts. Materials. 2018;11:1322. doi:10.3390/ma11081322.
68. Tian X, Liu T, Yang C, Wang Q, Li D. Interface and performance of 3D printed continuous carbon fiber reinforced PLA composites. Appl Sci Manuf. 2016;88:198–205. doi:10.1016/j.compositesa.2016.05.032.
69. Pantani R, De Santis F, Sorrentino A, De Maio F, Titomanlio G. Crystallization kinetics of virgin and processed poly(lactic acid). Polym Degrad Stab. 2010;95(7):1148–59. doi:10.1016/j.polymdegradstab.2010.04.018.
70. Khosravani MR, Reinicke T. On the use of X-ray computed tomography in assessment of 3D-printed components. J Nondestr Eval. 2020;39(4):1–17. doi:10.1007/s10921-021-00818-1.